Chapter 4

CeO_2-mediated oxygen vacancy rich Co_3O_4 on graphene for enhanced oxygen reduction and evolution reaction in alkaline media

Outline

Among transition metal based catalysts, cobalt (Co)-based electrocatalysts have particularly gained attention due to the multivalent nature of cobalt, as well as its high abundance and low-cost, 10−15 USD/lb [1], compared with noble metals. Great amount of research has been dedicated towards improving the catalytic performances of spinel cobalt oxides (Co_3O_4) [2]. The shuttle between Co^{2+} *Td* and Co^{3+} *Oh* enables the Co_3O_4-based catalysts to be inherently bi-functional towards ORR and OER. Engineering the molecular and electronic structure of a generic Co_3O_4 by employing MO|MO (MO: metal oxide) interface is a versatile technology to boost its robustness [3]. The generation of a heterogeneous interface alters the band gap and provides a greater number of transient active sites in Co_3O_4 that allows facile electron transport for ORR and/or OER. One such electronic modulation is brought about by the incorporation of the ceria (CeO_2). CeO_2, a well-known oxygen buffer, proves to be a highly efficient additive in modifying the inherent catalytic activities of Co-based electrocatalysts. There are numerous reports on this [4–10] but not much is understood about the mechanistic details. A better understanding of the redox properties of Co_3O_4 upon incorporation of CeO_2 is key to developing highly efficient cheaper electrocatalysts as substitutes for Pt/C, RuO_2 and IrO_2. Since the 3d MO_x have high electrical resistance, using a conductive carbon support is preferred, resulting in a MO_x/C type composite [11].

In this work, we report the design of a solvothermally synthesized Co_3O_4/CeO_2/GNP (GNP: graphene nanoplatelets), which provides a means to engineer the interface of the crystalline/amorphous (semicrystalline) spinel Co_3O_4 towards ORR and OER in alkaline media. The graphitic-C promotes electrical conductivity in the support [12], whilst the flexible transformation between Ce^{3+} and Ce^{4+} in CeO_2 modifies the surface atomic ratio of Co^{2+} and Co^{3+} ions in Co_3O_4. This, in turn, modifies the adsorption affinity towards oxygen species and modifies the ORR and OER activity [13]. A systematic investigation has been carried out to study the underlying synergistic effects responsible for the higher catalytic performance of Co_3O_4/CeO_2/GNP compared to their non-hybrid analogues, Co_3O_4/GNP and CeO_2/GNP. The catalysts were tested for bi-functionality, long-term durability and stability to examine their practical application. The goal of the work was to develop an efficient and durable oxygen electrocatalyst and to contribute to the understanding of key factors to design a bi-functional catalyst.

The synthesis procedure of the catalysts Co_3O_4/GNP, CeO_2/GNP and Co_3O_4/CeO_2/GNP are described in Section 2.2.1, 2.2.3 and 2.2.4, respectively. Their physical characterization and electrocatalytic activities have been described below.

4.1 Results and discussion

4.1.1 Physical characterization of the catalysts

The as-synthesized materials were characterized by PXRD, Raman spectroscopy, TGA, BET surface area measurements, FTIR, ICP-OES, XPS, XANES and EXAFS spectroscopy, and TEM/HR-TEM.

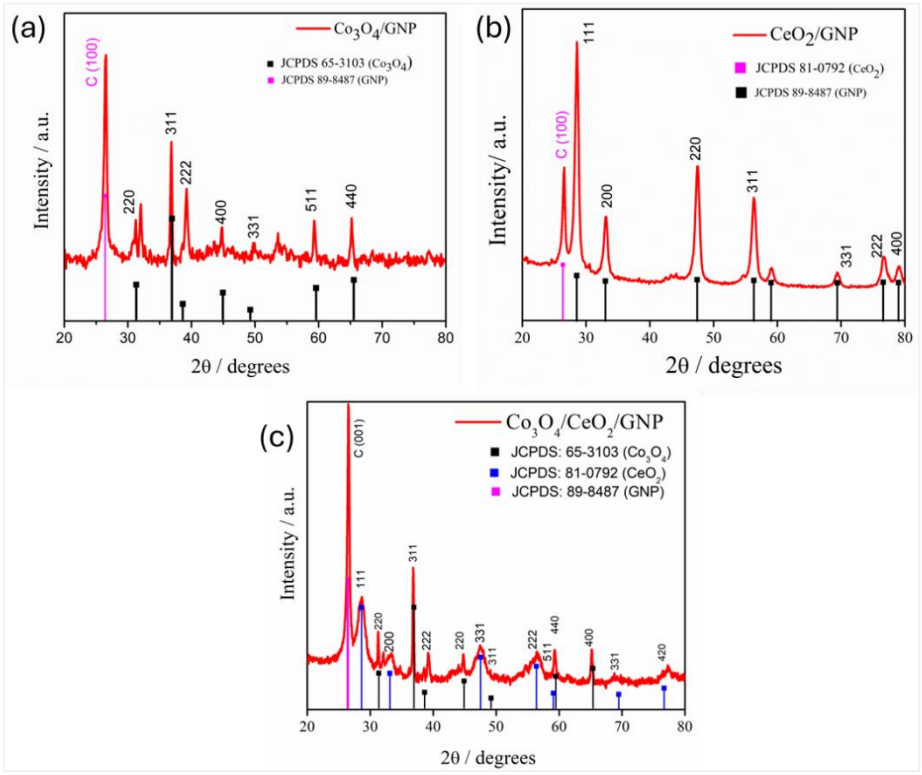

Figure 4.1. PXRD spectra of (a) Co_3O_4/GNP, (b) CeO_2/GNP, and (c) Co_3O_4/CeO_2/GNP.

The PXRD spectra of the catalysts are presented in Figure 4.1(a). The spectra correspond to JCPDS card nos. 65-3130 (for Co_3O_4; crystallizes in the cubic $Fd\bar{3}m$ space group), 81-0792 (for CeO_2; crystallizes in the cubic $Fm\bar{3}m$ space group) and 89-8487 (for GNP). The materials are polycrystalline. Co_3O_4, CeO_2 and GNP exhibit sharp diffraction peaks while Co_3O_4/CeO_2/GNP exhibit comparatively broader peaks, more prominently

from CeO_2. This indicates that Co_3O_4/CeO_2/GNP is not purely crystalline [14]. It is amorphous to some extent compared to its individual counterparts Co_3O_4, CeO_2 and GNP.

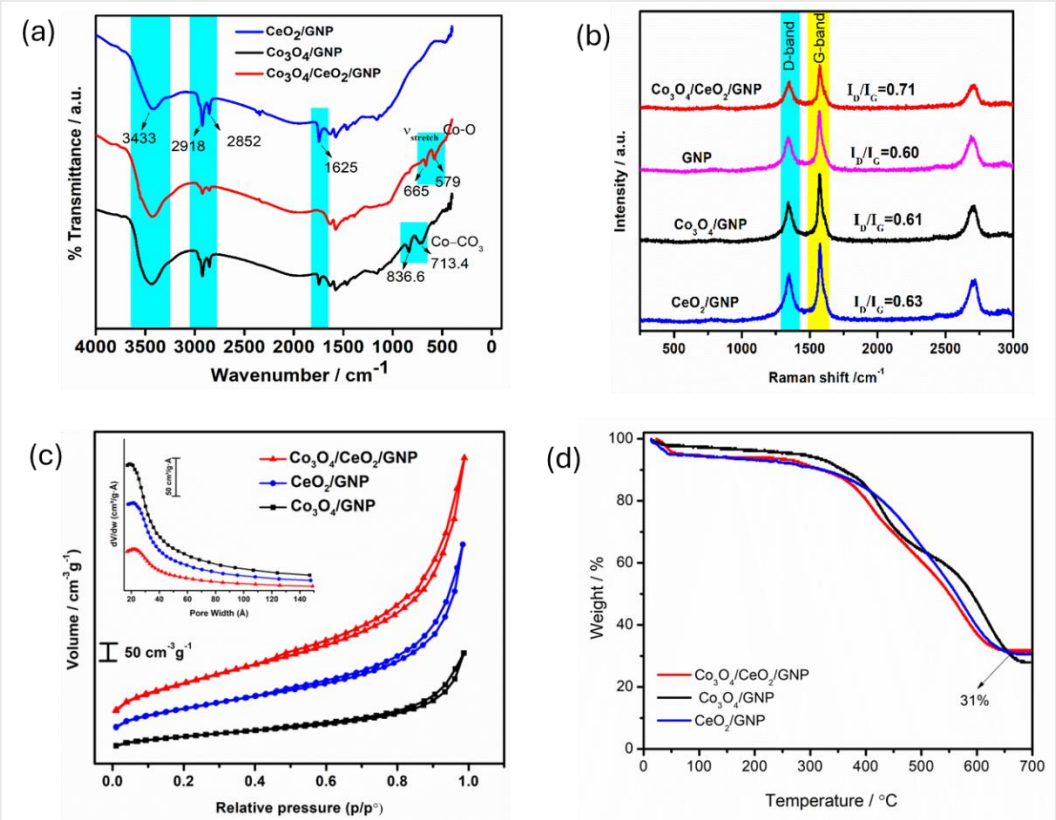

Figure 4.2. (a) FTIR spectra, (b) Raman spectra, (c) N_2 adsorption/desorption isotherms with BJH pore distribution (inset), and (d) TGA of various catalysts.

The FTIR spectra is presented in Figure 4.2 (a)**.** The strong and broad band at 3433 cm^{-1} arises from stretching vibrations of H-bonded O− H bonds from residual water molecules [15]. The two medium bands at 2918 cm^{-1} and 2852 cm^{-1} arise from the C−H stretching vibrations of the methylene groups (− CH_2−) in the defective graphene nanoplatelets. The weak band at 1625 cm^{-1} is for bending modes of water molecules [16]. In the Co_3O_4/CeO_2/GNP, the bands at 665 cm^{-1} and 579 cm^{-1} represent stretching frequencies $\nu_{stretch}$ of Co−O bonds in spinel Co_3O_4. The band at 665 cm^{-1} (ν_2) depicts the vibration of Co^{2+} ions in Td holes and the one at 579 cm^{-1} (ν_2) represents vibration of Co^{3+} ions in Oh holes [15,17]. However, these two bands are very less prominent in the spectrum for Co_3O_4/GNP and instead, two prominent bands are observed at ~836 cm^{-1} and 718 cm^{-1} respectively which indicates presence of surface Co − OH bonds [18] and/or ν_2

(A''_2) and ν_4 (E'') respectively corresponding to normal modes of vibration of planar CO_3^{2-} molecules/ions [19]. This might be due to presence of trace amounts of $CoCO_3$ that tend to precipitate out in similar urea-based solvothermal synthesis technique as reported in [20] and only converts into pure phase Co_3O_4 when the supernatant liquid is allowed to further precipitate and annealed at high temperatures.

Raman spectra are presented in Figure 4.2 (b). The as-synthesized catalysts display sharp response for D-band at ~1353 cm^{-1}, for G-band at ~1582 cm^{-1} and for 2D band at ~2700 cm^{-1}. The intensities of the D-band depict the presence of sp^3 defects in the carbon lattice comprising the graphene nanoplatelets while the G-band reflects E_{2g} phonons arising out of in-plane stretching modes [21]. The I_D/I_G intensity ratios were calculated as this value is indicative of the extent of defects in the overall structure. It is observed that the I_D/I_G value is the highest for Co_3O_4/CeO_2/GNP (0.71) while that for Co_3O_4/GNP, CeO_2/GNP and GNP are ~0.6. This indicates that there are ~17% more defects in the overall structure of Co_3O_4/CeO_2/GNP.

Powdered samples are rarely smooth at the atomic level. To determine the textural porosity of the catalysts, N_2 gas adsorption isotherms were measured. Prior to measurement, the catalysts were degassed at 80 °C for 1 h and 120°C for 3 h under vacuum to remove moisture and any possible contaminants. The adsorption/desorption curves are presented in Figure 4.2 (c). The isotherms exhibit Type IV curves with an H3 hysteresis loop. This indicates the presence of capillary condensation and slit-like pores [22,23]. This feature is attributed to non-rigid aggregates of partially exfoliated stacks of the graphene nanoplatelets in the catalysts. The pore size distribution curve from the adsorption isotherm employing the BJH model is also shown in inset of Figure 4.2 (c). The average pore width of the catalysts fall in the range of 41− 43 Å (~4 nm), indicating that the catalysts are mesoporous in nature. The average pore volumes are similar (~0.25 cm^3/g) for the three catalysts. The total specific surface areas as calculated from the BET equation are listed in Table 4.1 and follows the order: Co_3O_4/CeO_2/GNP < Co_3O_4/ GNP < CeO_2/GNP.

Table 4.1: BET surface area, pore width and pore volume of the catalysts.

Catalysts	BET specific surface area ($m^2\ g^{-1}$)	Av. pore width (Å)	Av. Pore volume (cm^3/g)
$Co_3O_4/CeO_2/GNP$	250	41.2	0.25
Co_3O_4/GNP	264	42.5	0.26
CeO_2/GNP	271	43.3	0.27

TGA was performed to confirm the 30:70 wt% ratio of catalyst to GNP. This is presented in Figure 4.2 (d). About 2− 4 mg of the catalysts were heated under air atmosphere with a temperature ramp of 10 °C min^{-1} up to 700 °C. A slight decrease in weight was observed in all the catalysts ~100 °C which is due to removal of adsorbed water molecules. The weight% comes down to ~30% of the initial weight which ensures the 30:70 catalyst to graphene loading. The TGA curve for Co_3O_4/GNP shows a two-step decomposition revealing the presence of some amount of cobalt hydroxide that gets oxidized at ~300°C to Co_xO and this Co_xO upon heating again rearranges to Co_3O_4 [24] as well as presence of carbonates that decompose in the range of 320−450° [19].

To confirm the correct loading of the metals, the ICP-OES analysis of the $Co_3O_4/CeO_2/GNP$ catalyst was conducted, and the ratios are tabulated in Table 4.2.

Table 4.2. Atomic wt.% in $Co_3O_4/CeO_2/GNP$ determined from ICP-OES.

Sample	Element	Results in wt.%	Co/Ce wt.% from ICP-OES	Co/Ce atomic ratio
$Co_3O_4/CeO_2/GNP$	Ce	6.96	1.3	3:1
	Co	9.11		

From wt.% in Table 4.2, we confirm that the atomic ratio of Co/Ce is maintained at 3:1. The Co/Ce ratio is further confirmed by Energy-Dispersive X-ray Spectroscopy (EDX) analysis (Figure 4.3).

EDS analysis was done on $Co_3O_4/CeO_2/GNP$ at two different areas to see the atomic distribution and elemental composition of the individual atoms Co, Ce, O and C, on a JEOL, JAPAN (Model: JSM 6390LV) instrument. The spectra resulting from the selected areas of the catalyst image reveals an average of Co/Ce = (2.5 + 4)/2 = 3.2

atomic% ratio which assures that all of the starting materials have been incorporated in the correct ratio. The average atomic% of carbon (86.37 + 82.77)/2 = 84.57 % is higher than the 70% loading which is possibly because of residual carbon atoms from the graphite tap on the stub used to mount the catalyst. From the individual maps, it is seen that Ce atoms were more evenly distributed all over the region while Co was only sparsely distributed and mostly agglomerated as globules.

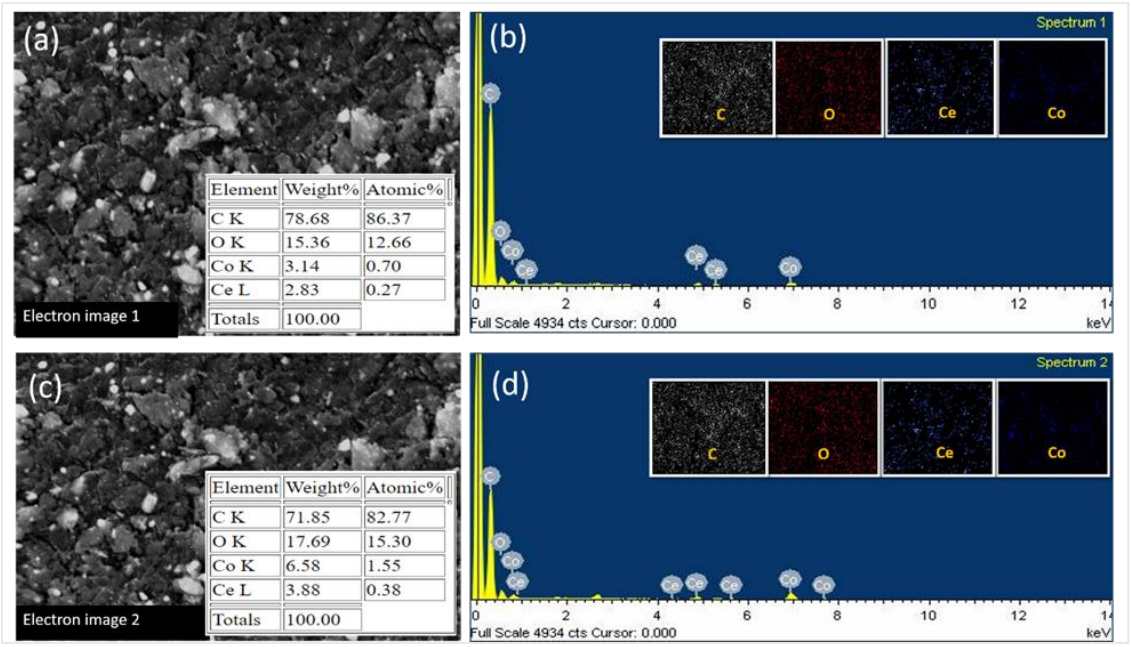

Figure 4.3. EDX-elemental mapping of the atoms C, O, Co and Ce for the catalyst Co_3O_4/CeO_2/GNP for two electron images (a,c) with the composition tables shown in insets, (b,d) corresponding spectra from elemental mappings. The elemental maps are shown in insets of (b,d).

TEM and HR-TEM micrographs were taken to examine the microstructure of the particles which is presented in Figure 4.4. Figure 4.4 (a) reveals loosely bound aggregates. This observation is consistent with an H3 hysteresis loop observed in N_2 adsorption/desorption isotherm shown in Figure 4.2 (c). Empty spaces (voids and crystal defects) and grain boundaries observed between crystallites are seen in Figure 4.4 (e,f). The selected area electron diffraction pattern (SAED) is typical of polycrystalline material with overlapping rings (see Figure 4.4 (c)). The average size of the particles is 6.5 nm. Using the TEM image shown in Figure 4.4 (d), the nanoparticle size distribution histogram was determined using ImageJ software [25] by selecting 26 randomly distributed particles.

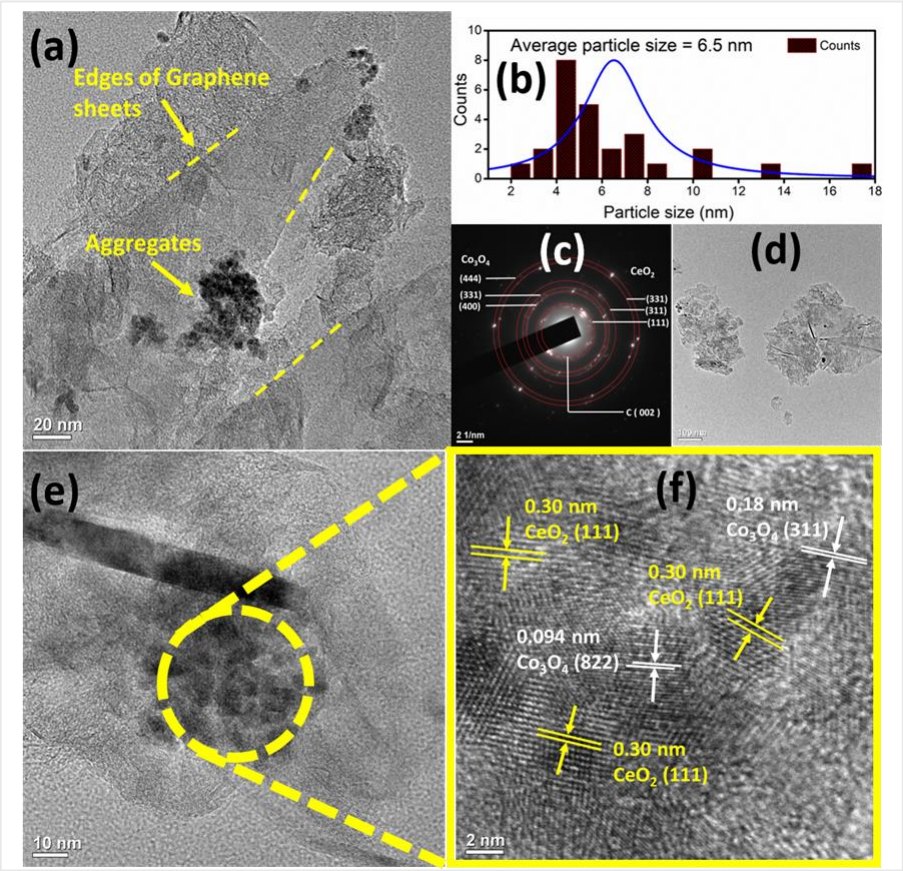

Figure 4.4. (a) HR-TEM image of Co_3O_4/CeO_2/GNP showing loosely bound aggregates on graphene sheets (b) Histogram for particle size distribution (c) SAED pattern with concentric rings indexed to corresponding Miller planes (d) low resolution TEM image used to determine particle size distribution and (e) HR-TEM image showing different crystallites of Co_3O_4 and CeO_2 with lattice fringes indexed in (f).

To know more about the surface chemical composition of the catalysts, XPS was carried out on the as-synthesized catalysts. All peaks were deconvoluted using Gaussian fitting. The core level O 1s spectra of the three catalysts were deconvoluted into three distinct peaks (see Figure 4.5 (a)); at 532.8 eV (for surface adsorbed oxygen or hydroxyl groups comprising possibly of $Co(OH)_2$ represented as O_{ads} at 531.5 eV for low-coordinated surface oxygen-deficient species (O_v), and at 530 eV for those bounded to metal atoms or lattice oxygen (O_{lat}) [4,15,26]. The fractional percentages of O_{ads}, O_v and O_{lat} are calculated from the area integration of the deconvoluted peaks using the formula:

$$\% \, O_v = \frac{[O_v]}{[O_{ads}] + [O_v] + [O_{lat}]}$$

The comparison of relative oxygen vacancies in the three catalysts is shown in the bar diagram of Figure 4.5 (b). It was found that the mixed catalyst $Co_3O_4/CeO_2/GNP$ has the highest fraction of oxygen vacancies (68%) as presented in the bar diagram in Figure 4.5 (b). This is accompanied by 23% of Ce^{3+} ions and an almost 1:1 ratio of Co^{2+}/Co^{3+} (i.e. 52% : 48%, see Table 4.3) to balance the charge neutrality.

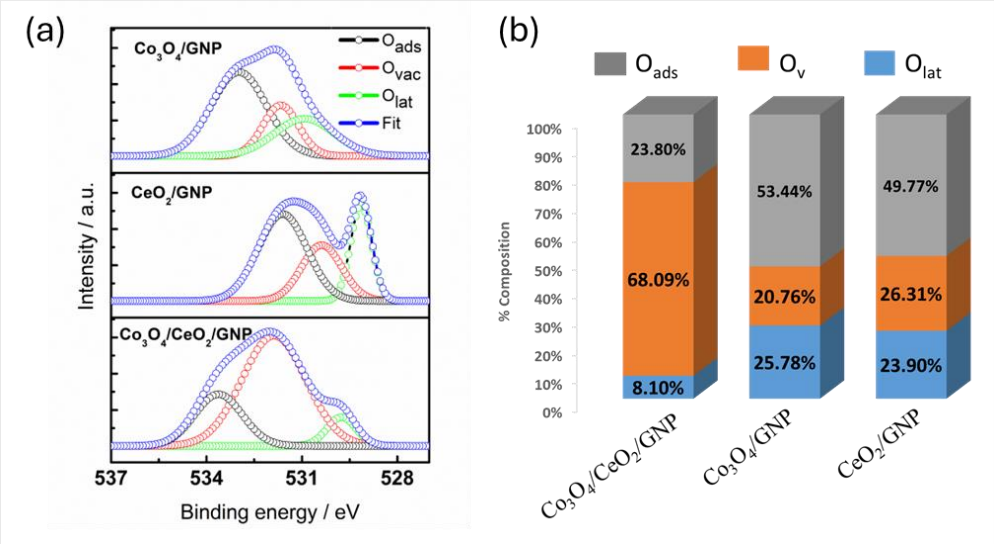

Figure 4.5. (a) Core O 1s XP spectra, and (b) bar diagram representing %composition of O_{ads}, O_v and O_{lat} in the as-synthesized catalysts.

The wide range survey spectrum $Co_3O_4/CeO_2/GNP$ and its core XP spectrum for C, Co and Ce are presented in Figure 4.6. The core-level Co 2p XP spectra of $Co_3O_4/CeO_2/GNP$ (Figure 4.6 (c)) show two spin-orbit doublets with 15.8 eV apart; a high energy doublet band at 797.5 eV for Co $2p_{1/2}$ and a low energy doublet band at 781.7 eV for Co $2p_{3/2}$, accompanied by two satellite peaks. The spin-orbit splitting energy difference of 15.8 eV is a characteristic of cubic Co_3O_4 [17]. The satellite peak at 804.5 eV for Co $2p_{1/2}$ and another one at 789.1 eV for Co $2p_{3/2}$ are characteristics of spinel Co_3O_4 [27]. The low energy doublet band at 781.7 eV could be deconvoluted into two fitting peaks (784.7 eV and 781.5 eV), representing Co^{2+} and Co^{3+} respectively. Similarly, the high energy band at 797.5 eV could be deconvoluted into two fitting peaks, at 798.7 eV and 797.3 eV, representing Co^{2+} and Co^{3+} respectively. The relative% of Co^{2+} and Co^{3+} as calculated from the area under the fitted peaks are found to be 52% and 48% respectively. The details of the Co 2p XP spectra are listed in Table 4.4. The area ratio of Co^{2+} is higher than Co^{3+}, indicating the non-stoichiometric distribution of the Co^{2+} *Td* and Co^{3+} *Oh* from the generic spinel formula AB_2O_4. The Ce 3d core-level XPS spectra were deconvoluted into eight

sub-peaks shown in Figure 4.6 (d). All details obtained from the Ce 3d XP spectra are listed in Table 4.3.

Table 4.3: Peak positions and relative % of Ce^{3+} and Ce^{4+} in Ce 3d XP spectra Co_3O_4/CeO_2/GNP.

Doublet	**Species**	**Peak notations**	**Peak position / eV**	**% Ce^{3+}**	**% Ce^{4+}**
Ce $3d_{3/2}$	Ce^{3+}	u'	902.8	23.3 %	76.7 %
	Ce^{4+}	u	917.2		
		u''	907.7		
		u'''	901.2		
		v'''	898.8		
Ce $3d_{5/2}$	Ce^{3+}	v''	889.2		
	Ce^{4+}	v	882.8		
		v'	885.3		

Out of these eight, u' and v'' represent the $3d^{10}4f^1$ electronic configuration of Ce^{3+} $3d_{3/2}$ and $3d_{5/2}$ respectively, while the rest represent the $3d^{10}4f^0$ electronic configuration of Ce^{4+} ions [15,28]. The u' and v'' peaks are significant which implicates the presence of the substantial amount of Ce^{3+} ions on the surface. The Ce^{3+}/Ce^{4+} ratio is a crucial parameter that correlates greatly with its catalytic efficiency due to oxygen non-stoichiometry. This ratio depends greatly on the synthesis technique. Obtaining the desired ratio is a challenging task and is not very well understood [29]. The presence of both Ce^{3+} and Ce^{4+} proves the inherent redox nature of CeO_2 and it is an indication of charge imbalance and oxygen vacancies in the Co_3O_4/CeO_2/GNP catalyst.

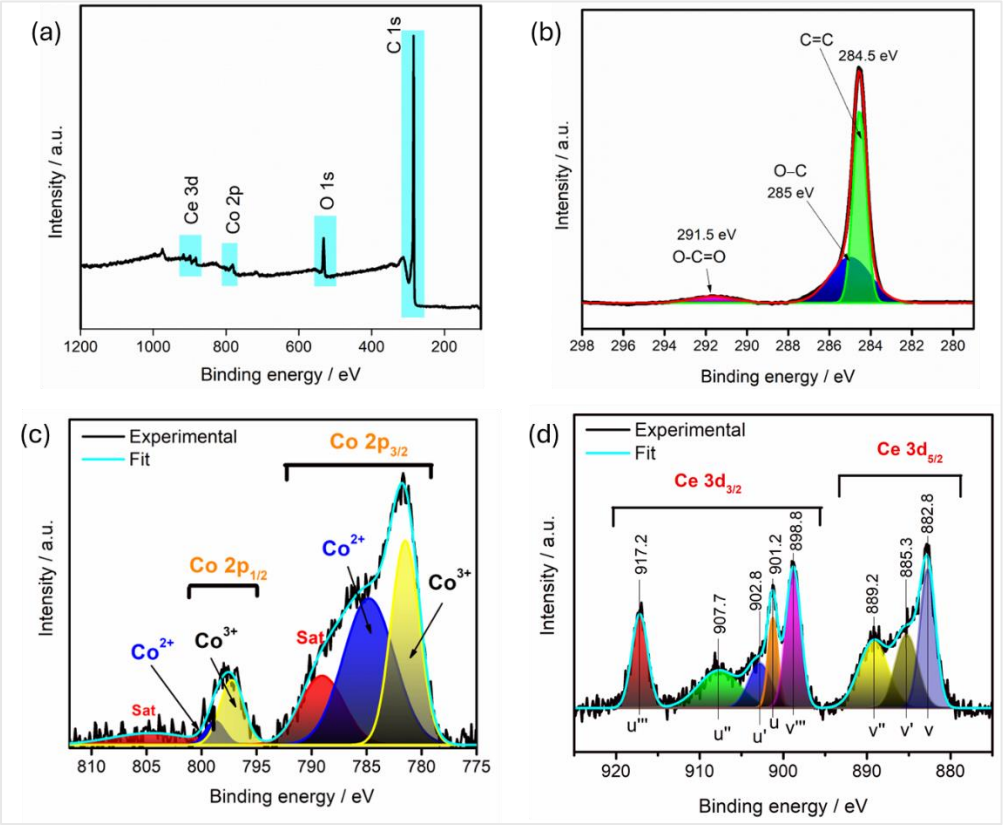

Figure 4.6. (a) Wide range survey spectrum, (b) C 1s XP spectrum, (c) Co 2p XP spectrum, and (d) Ce 3d XP spectrum of Co_3O_4/CeO_2/GNP.

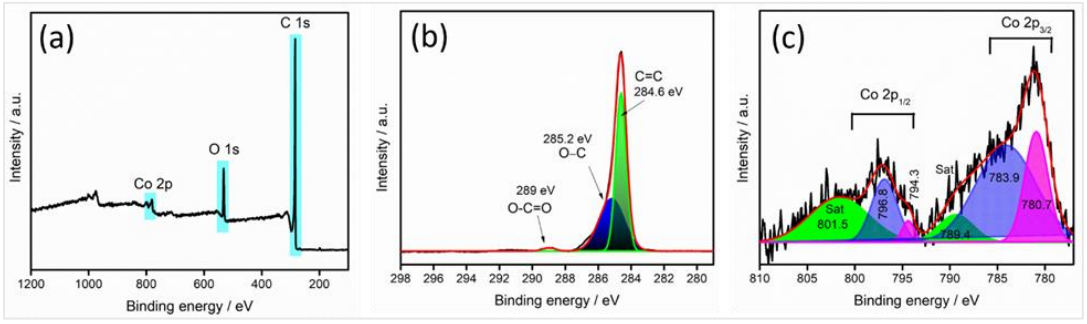

Figure 4.7. (a) Wide range survey spectrum, (b) C 1s spectra, and (c) Co 2p core spectra of Co_3O_4/GNP.

Similarly, the survey spectra of Co_3O_4/GNP and CeO_2/GNP are also presented along with core XP spectra of the individual atoms present are also presented in Figures 4.7 and 4.8 respectively. From Table 4.4, it is observed that binding energies of Co ions have a more positive shift in the mixed catalyst Co_3O_4/CeO_2/GNP which confirms that bonds in Co_3O_4/CeO_2/GNP are stronger than those in Co_3O_4/GNP.

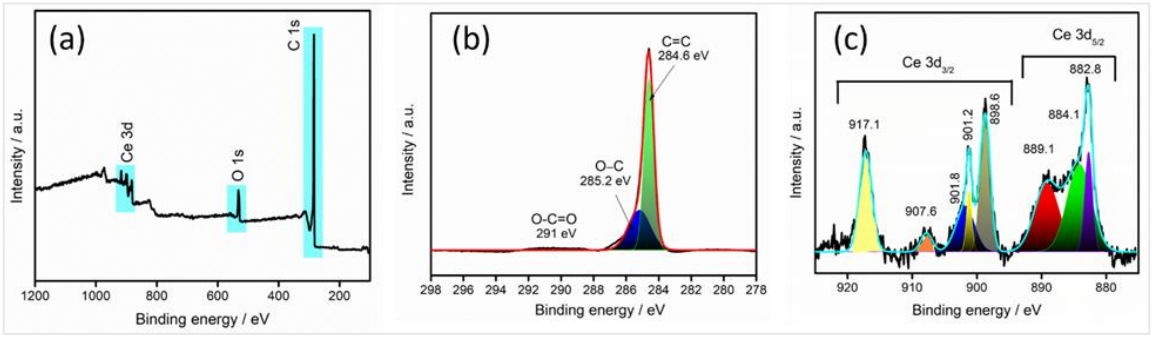

Figure 4.8. (a) Wide range survey spectrum, (b) C 1s spectra and (c) Ce 3d core spectra of CeO_2/GNP.

Table 4.4: Peak positions and relative % of Co^{2+} and Co^{3+} in Co 2p XP spectra of Co_3O_4/CeO_2/GNP and Co_3O_4/GNP.

Catalyst	Doublet	Peak notation	B.E. / eV	Relative % of Co^{2+}	Relative % of Co^{3+}
Co_3O_4/CeO_2/GNP	Co $2p_{1/2}$	Co^{2+}	798.7	52%	48%
		Co^{3+}	797.3		
	Co $2p_{3/2}$	Co^{2+}	784.7		
		Co^{3+}	781.5		
Co_3O_4/GNP	Co $2p_{1/2}$	Co^{2+}	796.8	72.35%	27.64%
		Co^{3+}	794.3		
	Co $2p_{3/2}$	Co^{2+}	783.9		
		Co^{3+}	780.7		

It is to be noted that the %composition of Co^{2+} ions are higher in Co_3O_4/GNP (72.35%) than that in Co_3O_4/CeO_2/GNP (52%) owing to presence of trace amounts of $Co(OH)_2$ and $CoCO_3$ as concomitant with FTIR spectra in Figure 4.2 (a).

For in-depth information regarding oxidation states and crystal structure, XANES and EXAFS regions obtained from XAS were evaluated carefully. The catalysts were mixed with cellulose and shaped into pellet form for the experiment as shown in Figure 4.9 (a). The obtained XAS data are presented in Figure 4.9 (b). The XANES data are normalized using software ATHENA and the k^2-weighted EXAFS data were fitted using ARTEMIS [30,31].

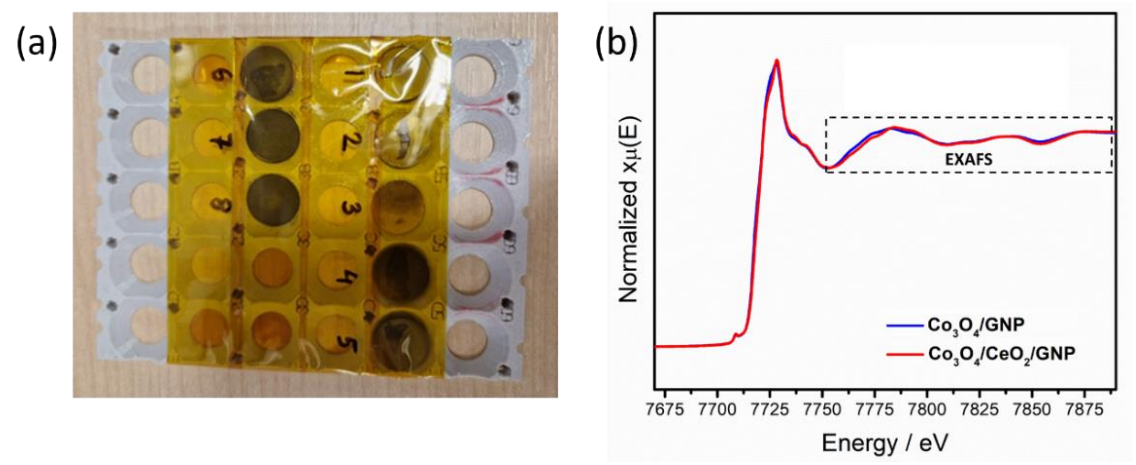

Figure 4.9. (a) Cellulose supported pellets on pellet rack for ex-situ XAS studies on B18 beamline at Diamond Light Source synchrotron facilities, (b) XAS of $Co_3O_4/CeO_2/GNP$ and Co_3O_4/GNP with EXAFS region marked.

Figure 4.10 (a) reveals observable differences between the Co K-edge XANES features of the three standards− Co, CoO, Co_3O_4 and the as-synthesized catalysts $Co_3O_4/CeO_2/GNP$ and Co_3O_4/GNP. The white line (1s → 4p) which appears around 7728 eV [32] of $Co_3O_4/CeO_2/GNP$ has a positive shift compared to Co_3O_4/GNP (see Figure 4.10 (b)). The position of pre-edge (1s → 3d) is the same for both, i.e. 7709 eV but the intensity is greater for $Co_3O_4/CeO_2/GNP$ (see Figure 4.10 (c)), which indicates that $Co_3O_4/CeO_2/GNP$ has slightly more distorted octahedral, making the spin forbidden 1s → 3d transition a little more pronounced.

To qualitatively determine the average oxidation state of cobalt in $Co_3O_4/CeO_2/GNP$ and Co_3O_4/GNP, the XANES of standards- Co foil, CoO and Co_3O_4 were used [33]. The linear plot of oxidation states vs. edge energies is shown in Figure 4.10 (e). The straight line follows the empirical relation $E_0 = (3.85 \pm 0.16).\ x + (7708.9 \pm 0.32)$ where E_0 is the main edge energy and 'x' is the average oxidation state of Co. Using this calibration plot, the average oxidation state of cobalt in Co_3O_4/GNP and $Co_3O_4/CeO_2/GNP$ are 2.28 and 2.38, respectively. The EXAFS data were fit to a three-shell model to investigate possible perturbation of the local coordination environment of the Co (see Figure 4.10 (d)). The simulated fitting parameters are presented in Table 4.5). However, not much difference was found, suggesting that the oxygen vacancies found via XPS may be restricted to the surface of the Co_3O_4 particles and, when CeO_2 is present with the ceria.

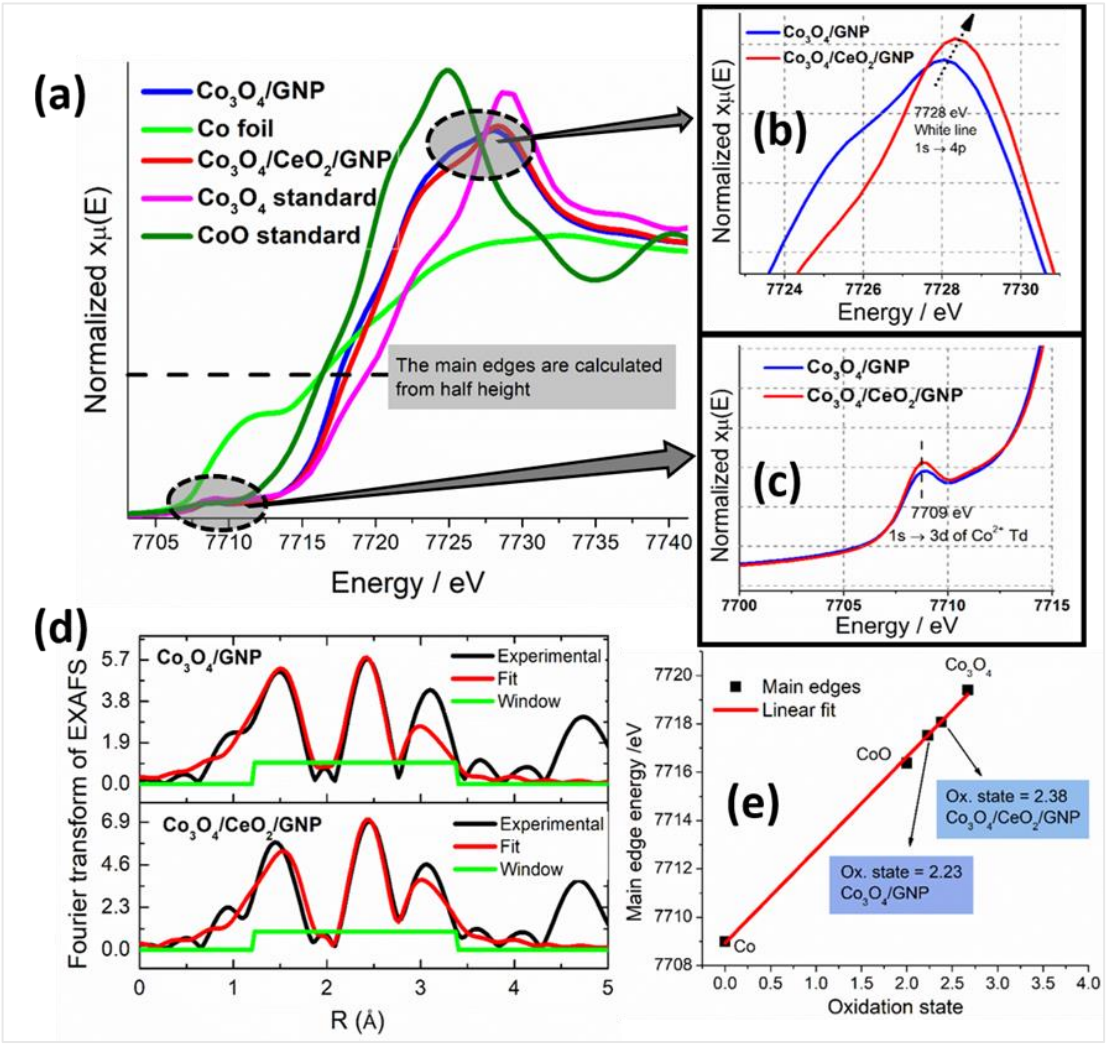

Figure 4.10. (a) Overlay of XANES of three standards− Co, CoO, Co_3O_4 and the as-synthesized catalysts Co_3O_4/CeO_2/GNP and Co_3O_4/GNP (b) white line region and (c) pre-edge region of Co_3O_4/CeO_2/GNP and Co_3O_4/GNP (d) k^2-weighted Fourier transform of Co K-edge EXAFS and their 1st shell fits obtained with R =1.2−3.4 Å (e) Linear plot of edge energy vs. oxidation states.

Table 4.5. Summary of 1st shell fitting of Co K-edge and the simulated parameters like Co-ordination number (N), Bond-length (R), Debye-Waller factor (σ^2), and inner potential shift (ε_o). R-factor represents goodness of fit.

Catalysts	Shell	N	R (Å)	σ^2 (Å^2)	R-factor
Co_3O_4/CeO_2/GNP	Co ─ O	12	1.953 ± 0.07	0.016	0.04
	Co ─ Co	12	3.360 ± 0.12	0.014	
	Co ─ Co	4	3.509 ± 0.12	0.006	
Co_3O_4/GNP	Co─ O	12	1.948 ± 0.07	0.018	0.08
	Co ─ Co	12	3.350 ± 0.13	0.018	
	Co ─ Co	4	3.499 ± 0.13	0.009	

4.1.2 Electrocatalytic study

A homogeneous suspension of the catalyst was prepared by ultrasonicating 5 mg sample with 500 μL each of water, isopropanol and 0.5 wt.% Nafion solution. A fine monolayer of 3 μL of the suspension was dropcasted onto a finely polished 3 mm diameter (disk area 0.0706 cm^{-2}) GC-RDE. This makes a catalyst loading of 0.142 mg cm^{-2}. The droplet was allowed to dry overnight at 35 °C in the oven under N_2 conditions.

A standard three-electrode electrochemical glass cell was used. A freshly prepared 3 M KCl filled Ag/AgCl as RE, a glass electrode with a clean Pt mesh at the tip as counter electrode (CE) and the GC-RDE as the WE were used. The supporting electrolyte used was 0.1 M KOH. The electrochemical experiments like stationary cyclic voltammetry (CV) were carried out at scan rate of 10 mV s^{-1} and linear sweep voltammetry (LSV) at rotation rates 400, 900, 1600, 2500, 3600 rpm at 10 mV s^{-1}. An accelerated durability test (ADT) was done for Co_3O_4/CeO_2/GNP to compare the shift in half-wave potential ($E_{1/2}$) before and after 10,000 cycles of CVs. CA was performed at 1600 rpm to compare the stability of the catalyst with 20 wt.% Pt/C. UHP-N_2 was purged into the electrolyte for 20 min to ensure elimination of any unwanted dissolved gases. UHP-O_2 gas was then purged for 20 min to ensure saturation of the system with O_2 for ORR. The O_2 flow was maintained at the surface of the electrolyte to form a blanket of O_2 gas to avoid the dissolution of other gases from air. Before performing ORR/OER, numerous fast scans

were performed until the voltammograms looked reproducible. All experiments were carried out at room temperature (25 ± 2 °C).

The three as-synthesized catalysts $Co_3O_4/CeO_2/GNP$, Co_3O_4/GNP and CeO_2/GNP are ORR active with prominent reduction peak at ~0.8 V vs. RHE as seen from Figure 4.11. The respective LSVs of the as-synthesized catalysts at rotation rates 400−3600 rpm are shown in Figure 4.12. The CVs and LSVs of Pt/C and GNP are shown in Figure 4.13.

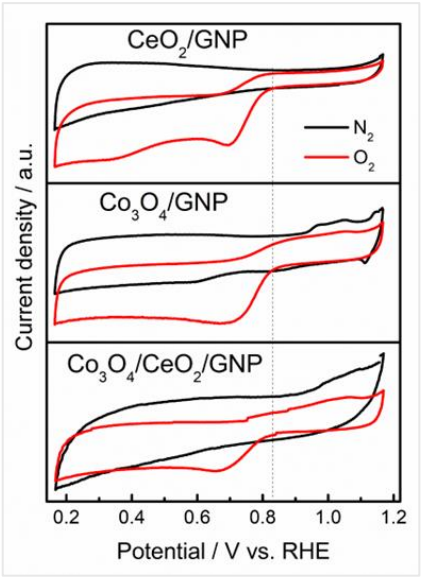

Figure 4.11. CVs of as-synthesized $Co_3O_4/CeO_2/GNP$, Co_3O_4/GNP and CeO_2/GNP under N_2 and O_2-saturated 0.1 M KOH at scan rate 10 mV s^{-1}.

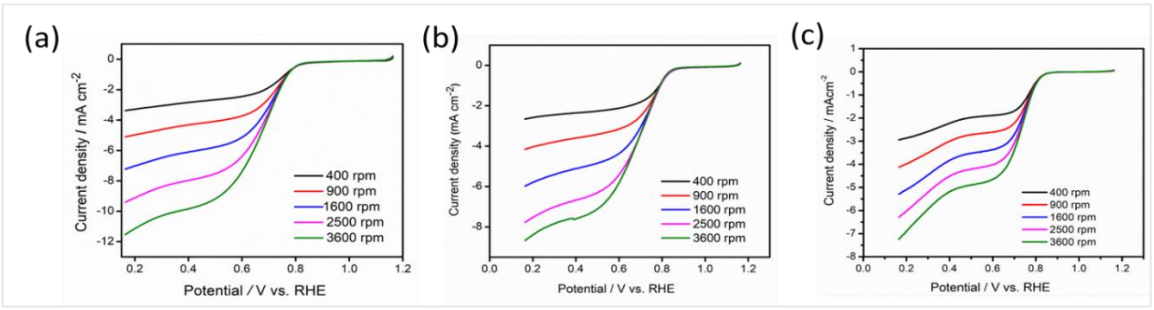

Figure 4.12. LSVs of (a) $Co_3O_4/CeO_2/GNP$, (b) Co_3O_4/GNP, and (c) CeO_2/GNP in O_2-saturated 0.1M KOH at 10 mV s^{-1}.

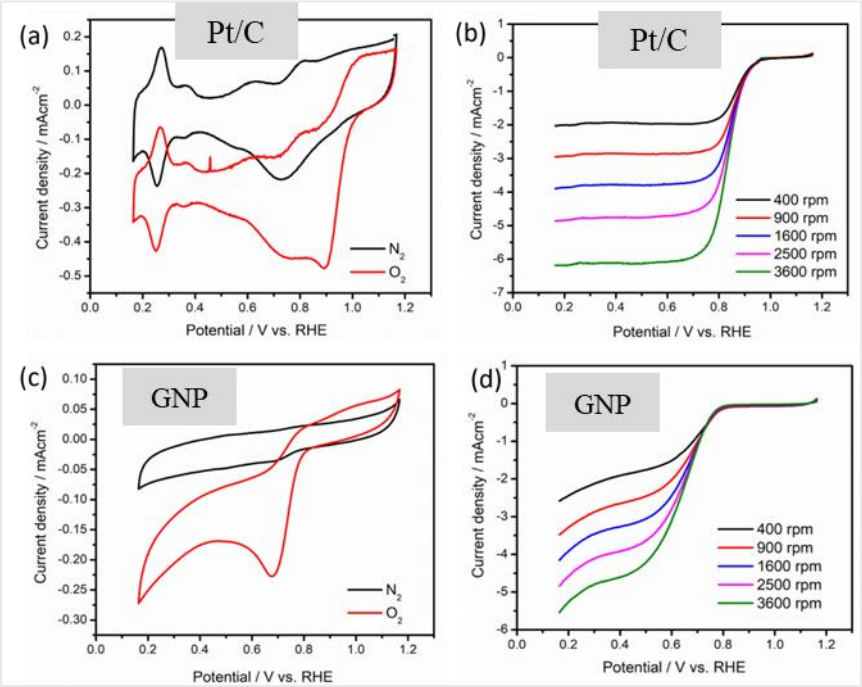

Figure 4.13. (a,c) CVs of Pt/C and GNP, and (b,d) LSVs of Pt/C and GNP, at 10 mV s^{-1}.

An overlay of the LSVs of the catalysts at 1600 rpm is shown in Figure 4.14 (a) with their respective current densities marked at potentials 0.2V, 0.4 V and 0.6 V. Another plot of $(i \times i_L)/(i_L - i)$ vs. E is also presented in Figure 4.14 (d) where i=current, i_L= limiting current, E= potential to provide a more correct comparison. This eliminates any error which might have come from residual ink drop cast or spillage beyond the effective geometric area of the GC-RDE. From Figure 4.14 (a) it is evident that all the studied catalysts exhibit a skewed baseline below 0.4 V, except Pt/C. This is most plausibly assumed to be a characteristic feature of the GNP as observed from Figure 4.13 (d). The skewed baseline is somewhat more pronounced in the case of CeO_2. So, this could also be a characteristic feature of CeO_2. The skewed baseline which starts appearing after an apparently short-lived plateau region at ~0.5V is indicative of extra components being reduced in addition to O_2. It is a common practice to compare the limiting current densities at 0.2V vs. RHE [8,34–41]. However, we propose that comparing them at any potential below 0.5 V (say 0.2V and 0.4 V in this case), might sometimes lead to erroneous interpretation. Hence, the geometric current densities at 0.6 V (the most appropriate region in this case) are considered as the limiting current densities for comparison to ensure more precision in the ORR study. In many cases, comparing the current densities at potentials beyond the ORR plateau region might deceive one in interpreting a catalyst to be superior to the commercial standard 20 wt.% Pt/C. Figure 4.14 (b) shows how comparing limiting

current densities at 0.2 V and 0.4 V (potential falling in the skewed region) deceives in making the Co_3O_4/CeO_2/GNP catalyst appear superior to that of 20 wt.% Pt/C.

Normalization of the limiting current density to the actual amount of metal-oxide is another way of expressing comparative electrocatalysis. The mass loading of all the catalysts is 10^{-2} mg corresponding to 3µL of ink deposited onto the working electrode. However, the active amount of catalyst for Pt/C is 20% while for Co_3O_4/GNP, CeO_2/GNP and Co_3O_4/CeO_2/GNP it is 30% of 10^{-2} mg. Accordingly, the mass specific activities are also calculated and shown in Figure 4.14 (c) which follows the order: Pt/C > Co_3O_4/CeO_2/GNP > Co_3O_4/ GNP > CeO_2/GNP > GNP. The mass-normalization method is done as explained in Section 2.6.9. The catalyst loading for the metal oxides (MO) is 30% of 0.142 mg cm^{-2} and 20% of 0.142 mg cm^{-2} for commercial 20 wt.% Pt/C.

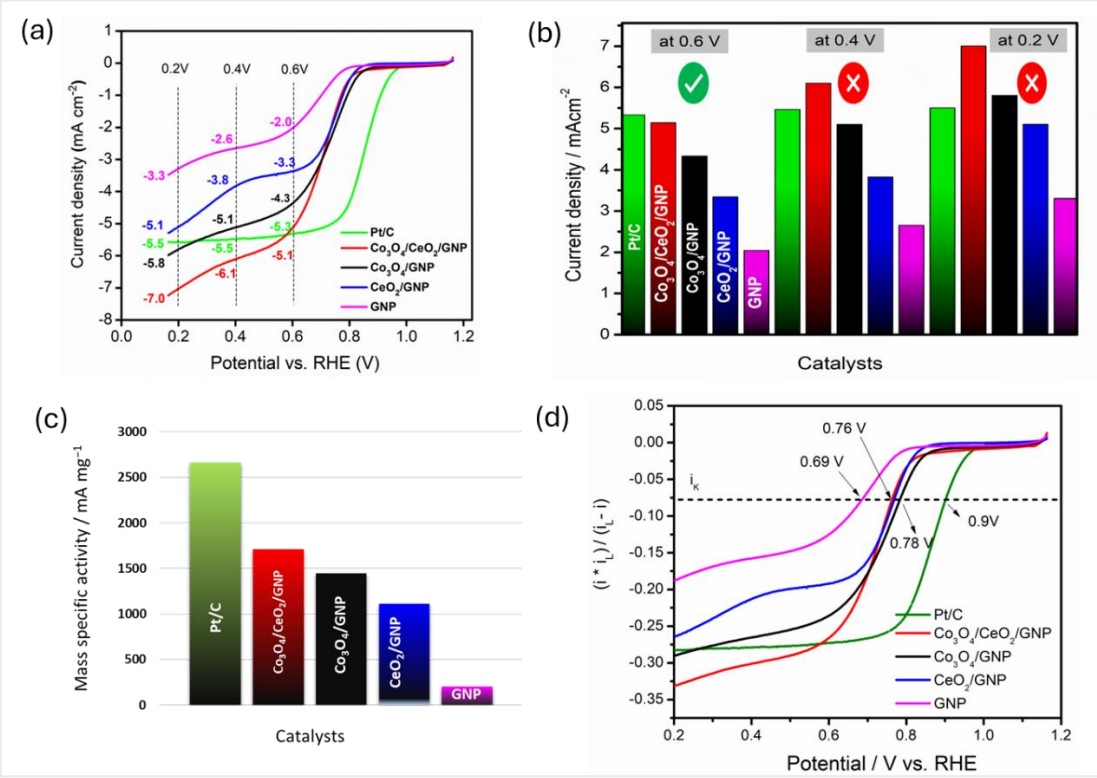

Figure 4.14. (a) LSVs of the catalysts at 1600 rpm with their current densities at 0.2 V, 0.4 V and 0.6 V marked, (b) Bar diagram representing current densities at 0.2 V, 0.4 V and 0.6V, (c) Bar diagram representing mass specific activities at 0.6V, and (d) Plot of $(i \times i_L)/(i_L - i)$ vs. E. Potentials for each catalyst to reach the target i_k are marked.

The ECSA is the area of an electrode that is accessible to the electrolyte for charge transfer and storage, and is considered to be an important feature of electrified interfaces [42]. It is derived from CVs at different scan rates as shown in Figure 4.15 (a–c) and the derived C_{DL} value is shown in Figure 4.15 (d–e).

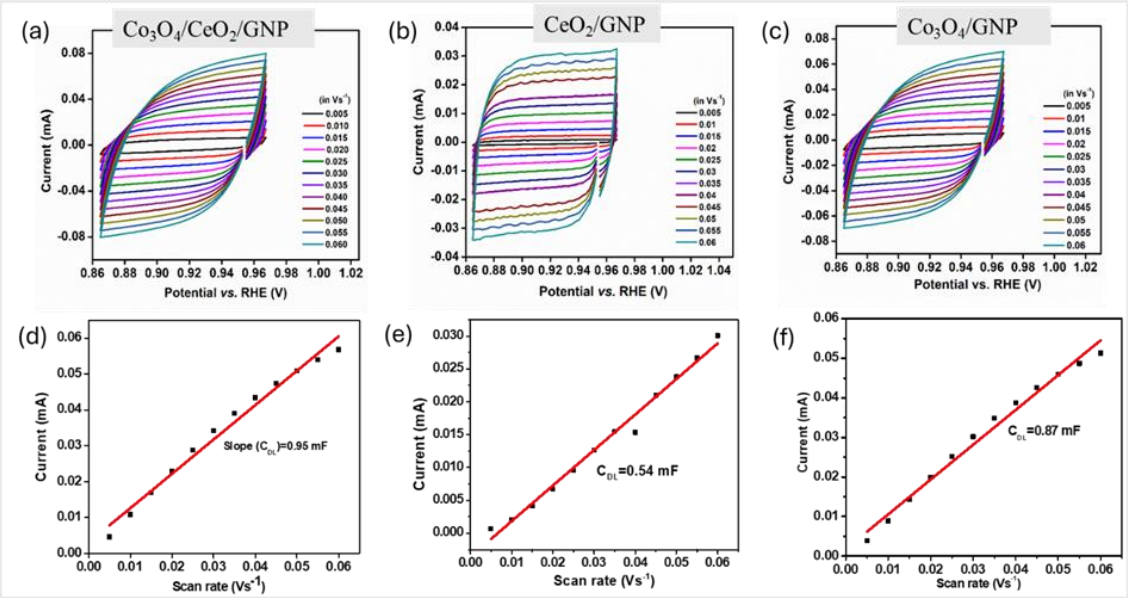

Figure 4.15. (a–c) CVs of the as-synthesized catalysts at different scan rates between 10–60 mV s^{-1}, and (d–e) Double layer capacitances (C_{DL}) derived from slope of charging current of the CVs.

The calculated mass-specific ECSAs (as shown in Figure 4.16) are in the order:

Co_3O_4/CeO_2/GNP (239.3) > Co_3O_4/GNP (219.9) > CeO_2/GNP (135.2) in $m^2\ g_{MO}^{-1}$. This decrease in ECSA could be correlated to the respective decrease in their current densities towards ORR (see Table 4.6). This is in reverse order to their mass-specific BET surface areas (shown in Figure 4.2 (c)). This is possibly due to the overlapping of Co_3O_4 and CeO_2 particles which blocks the internal pores of CeO_2 in the Co_3O_4/CeO_2/GNP mixed oxide. However, the reduced total specific surface area does not adversely affect the electrocatalytic activity of the mixed oxide.

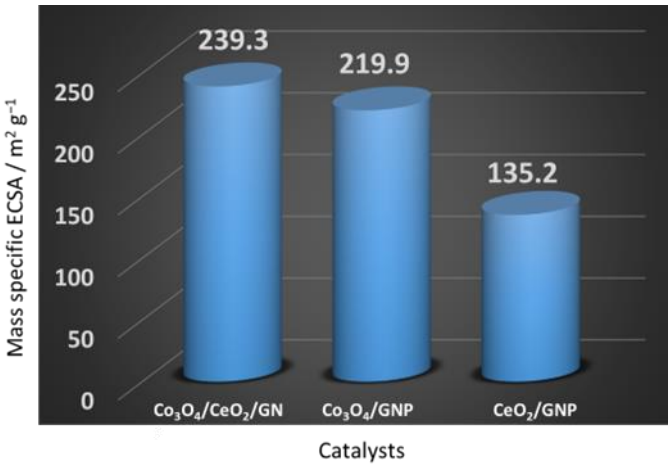

Figure 4.16. Bar diagram showing mass specific ECSAs.

The kinetics of these catalysts are analyzed by employing Koutecky-Levich (K-L) equation, assuming that K-L assumptions remain good in the mixed diffusion-kinetic region 0.5−0.75 V vs. RHE. The K-L plots are shown in Figure 4.17. Good linearity and parallelism are observed for Co_3O_4/CeO_2/GNP, Co_3O_4/GNP and CeO_2/GNP (Figure 4.17 (a−c)). For GNP, parallelism is observed only up to 0.7 V (Figure 4.17 (d)). The no. of electrons (*n*) transferred per mole of O_2 reduced are carefully derived from the slopes of K-L plots at potentials 0.5 V, 0.6 V, 0.7 V and 0.75 V, respectively. These are shown in the bar diagram in Figure 4.17 (e). While for the other catalysts, $2.5 < n \leq 3.5$, for Co_3O_4/CeO_2/GNP $3.5 < n \leq 4$, which is close to that of the commercial standard 20 wt.% Pt/C for a four-electron process (n=4), indicating the superior performance of the mixed oxide catalyst.

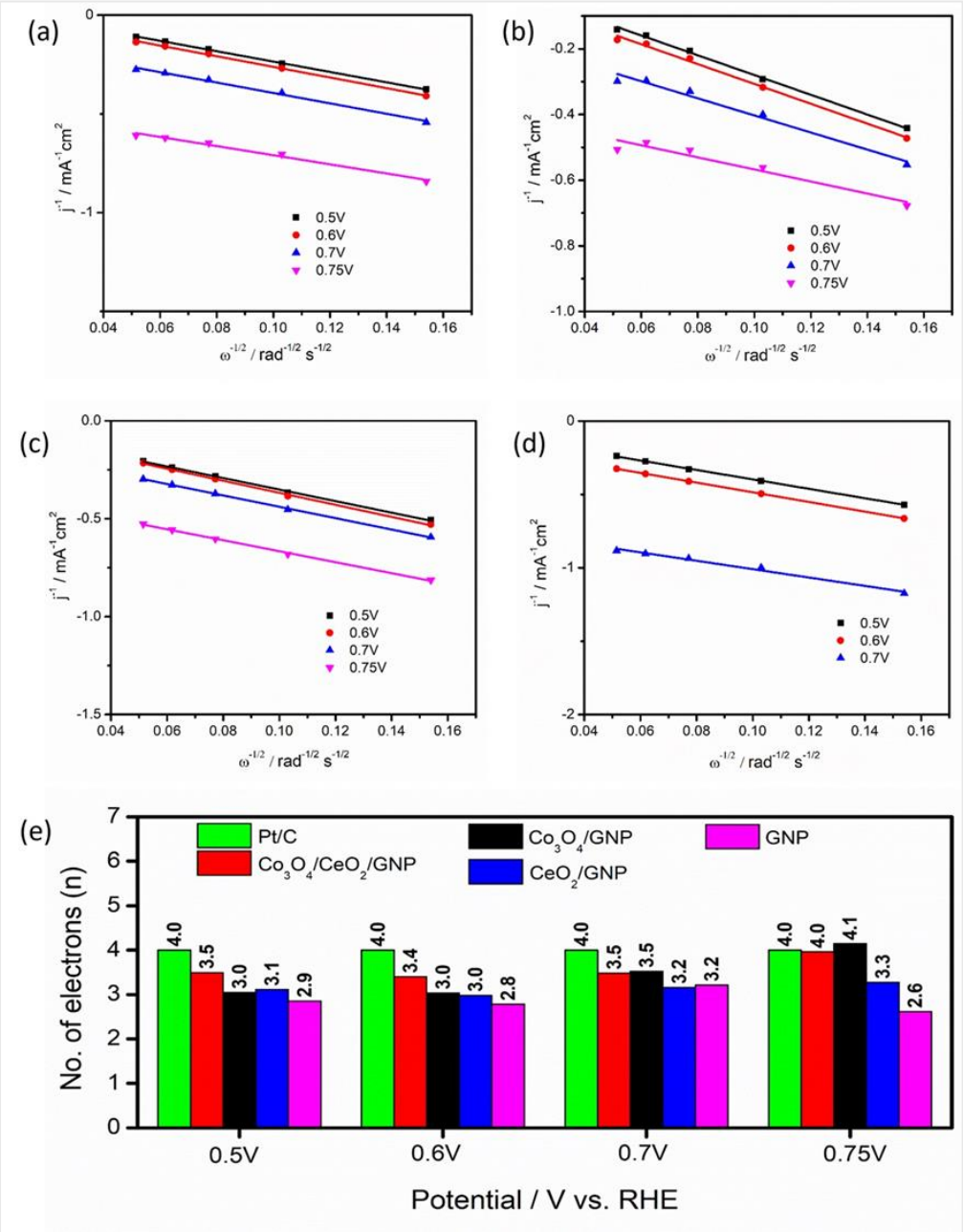

Figure 4.17. K-L plots for (a) Co_3O_4/CeO_2/GNP, (b) Co_3O_4/GNP, (c) CeO_2/GNP, (d) GNP and (e) number of electrons participating in ORR (n) in different potentials.

The stability of the Co_3O_4/CeO_2/GNP was explored via a chronoamperometric (CA) test, stepping the potential to 0.67 V, and an accelerated durability test (ADT). Following 10,000 rounds of the ADT, which involved cycling between 0.65 ─ 0.88 V at 500 mV s^{-1}, the LSVs are compared in Figure 4.8 (a). The minimal shift of 6 mV observed, indicates that Co_3O_4/CeO_2/GNP could be a promising candidate when it comes to long-term stability and commercialization. The CA test is expressed in %retention of current in

Figure 4.18 (b). The current retention of Co_3O_4/CeO_2/GNP is 87.6% compared to 72.5% for Pt/C.

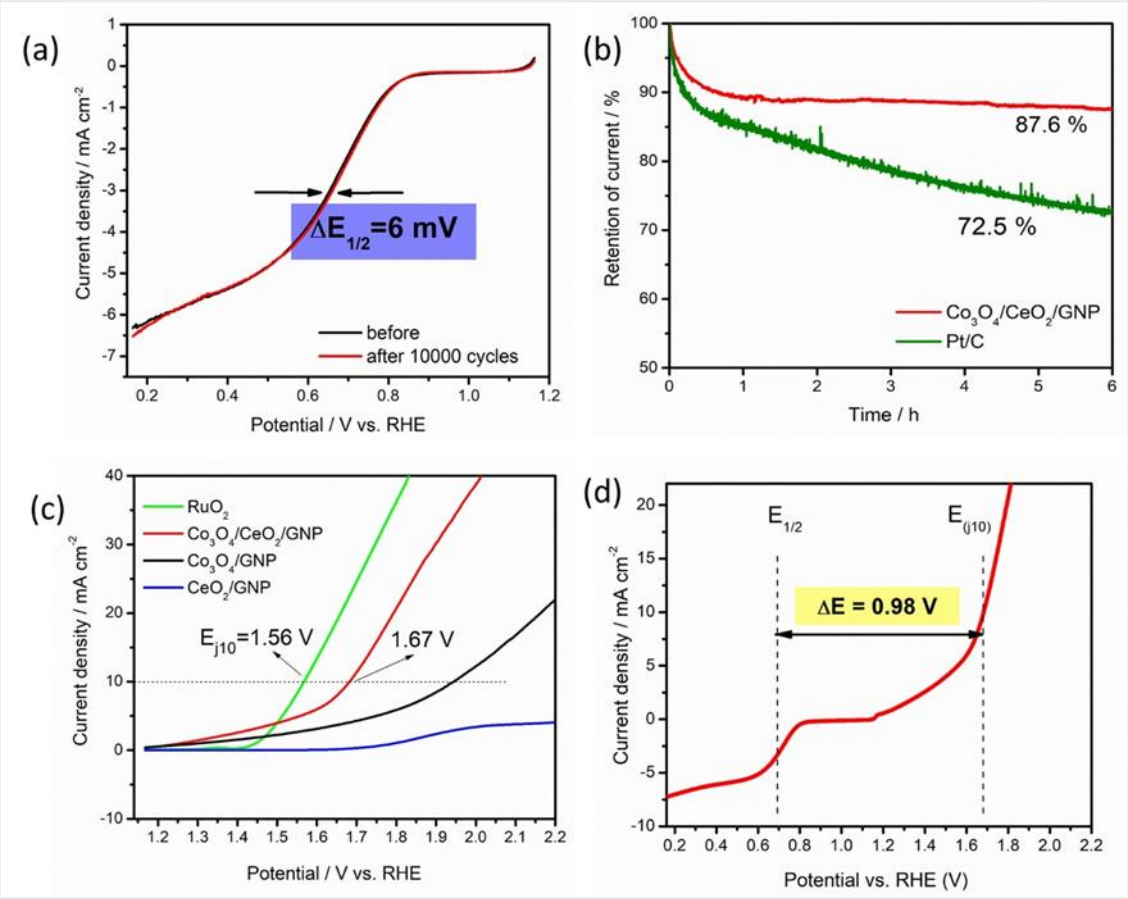

Figure 4.18. (a) LSVs of Co_3O_4/CeO_2/GNP before and after 10,000 CV cycles, (b) CA for current retention of Co_3O_4/CeO_2/GNP at potential 0.67 V vs. RHE, (c) LSVs of commercial standard RuO_2 and the as-synthesized catalysts Co_3O_4/CeO_2/GNP, Co_3O_4/GNP and CeO_2/GNP at 1600 rpm towards OER, and (e) bifunctionality index of Co_3O_4/CeO_2/GNP.

The catalysts were also tested for their performance towards OER. Similar to its performance in ORR, Co_3O_4/CeO_2/GNP has an earlier onset (1.64 V) than Co_3O_4/GNP and CeO_2/GNP which is obvious from Figure 4.18 (c). The potential to reach 10 mA cm^{-2} (E_{j10}) is a performance depicting parameter for OER activity. While the mixed oxide Co_3O_4/CeO_2/GNP has its E_{j10} at 1.67 V, the other two catalysts does not reach 10 mA cm^{-2} up to 2.2 V vs. RHE. The bifunctionality index is shown in Figure 4.18 (d). Table 4.6 summarizes all evaluated electrochemical parameters of the as-synthesized catalysts towards ORR/OER.

Table 4.6: The onset potentials ($E_{onset,ORR}$, $E_{onset,OER}$), geometric current densities for ORR at 0.6 V (j_{geo}), potential for 10 $mAcm^{-2}$ for OER (j_{10}) are listed below.*

Catalyst	$E_{onset,ORR}$/V	j_{geo} /$mAcm^{-2}$	$E_{onset,OER}$/V	j_{10}/V
Co_3O_4/GNP	+0.87	–4.33	+1.82	+1.94
CeO_2/GNP	+0.85	–3.34	+2.30	─
Co_3O_4/CeO_2/GNP	+0.85	–5.14	+1.64	+1.67
GNP	+0.80	–2.04	−	−
Pt/C	+1.00	–5.33	−	−
RuO_2	−	−	+1.41	+1.56

*Onset potentials are determined at the co-ordinates from which the flat line starts sloping downwards (for ORR) or upwards (for OER). $E_{onset,OER}$ for some catalysts are left blank as they are not functional for OER. Similarly, j_{10} of some catalysts are left blank as they failed to achieve 10 $mAcm^{-2}$ in the studied potential window.

Table 4.7 presents a list of similar cobalt-oxide based catalysts for comparison. Iis observed that the catalyst Co_3O_4/CeO_2/GNP reported in this work has an E_{onset} comparable to or slightly earlier than similar catalysts like Co_3O_4@Z67-N700@CeO_2 [12], Co_3O_4–CeO_2/C hybrid [15], CoO_x/CeO_2/RGO [43], Ag-CeO_2-Co_3O_4/C [8], Co_3O_4-NC/N-rGO [13] and Co_3O_4–CeO_2/KB [44]. Its half-wave potentials ($E_{1/2}$) are comparable to Co_3O_4–CeO_2/C hybrid [15], Co_3O_4-NC/N- rGO [13] and Oct-Co_3O_4/C [37]. The overpotential (η_{10}) of the catalyst is lesser than similar catalysts like Co_3O_4–CeO_2/C hybrid [15] and Co_3O_4/CeO_2@Co/N-CNF [10] while it is comparable to that of Co_3O_4-NC/N-rGO [13], Oct-Co_3O_4/C [37] and Co_3O_4@Pt/C nanofibers [46]. The bifunctionality index (ΔE) for the catalyst is slightly lesser than or comparable to those of Co_3O_4–CeO_2/C hybrid [15], Co_3O_4/CeO_2@Co/N-CNF [10], Co_3O_4-NC/N- rGO [13], Oct-Co_3O_4/C [37], Ag-CeO_2-Co_3O_4/C [8] and Co_3O_4@Pt/C nanofibers [46].

Table 4.7. Comparison of the performance recently reported Co_3O_4 -based electrocatalysts performance towards ORR/OER in 0.1 M KOH with our catalysts.

Catalyst	ORR		OER			References
	E_{onset} / V	$E_{1/2}$ /V	*$E(j_{10})$ / V	ΔE/V	*η_{10} /mV	
Co_3O_4/CeO_2/GNP	0.85	0.69	1.67	0.98	440	This work
Co_3O_4@Z67-N700@CeO_2	0.82		1.58	0.70	350	[12]
Co_3O_4−CeO_2/C hybrid	0.85	0.69	1.72	1.03	520	[15]
CoO_x/CeO_2/RGO	0.83		1.59	0.76	360	[43]
Ag-CeO_2-Co_3O_4/C	0.85		1.74	0.94	340	[8]
Co_3O_4/CeO_2@Co/N-CNF	0.88		1.84	1.09	570	[10]
Co_3O_4-NC/N- rGO	0.82	0.68	1.68	1.0	440	[13]
Oct-Co_3O_4/C	0.89	0.68	1.68	1.00	450	[37]
Co_3O_4@Pt/C nanofibers	0.90		1.67	0.93	442	[46]
Co_3O_4−CeO_2/KB	0.82					[44]

* Overpotential at 10 $mAcm^{-2}$ (η_{10}): $E(j_{10}) - 1.23$

* The bifunctionality index is mostly expressed as the potential window between $E(j_{10})$ for OER and $E_{1/2}$ for ORR: ΔE/V $[E(j_{10})-E_{1/2})]$

From the above results and discussion, it is observed that, the mixed oxide Co_3O_4/CeO_2/GNP exhibited a higher catalytic activity for both ORR and OER than Co_3O_4/GNP and CeO_2/GNP. This is attributed to the close contact of the two non-identical heterogeneous component oxides Co_3O_4/GNP and CeO_2/GNP that play complementary roles. The generation of a large number of point defects, namely oxygen vacancies, enables exposure of more active sites in Co_3O_4/CeO_2/GNP catalyst. The accessibility of active sites in Co_3O_4/CeO_2/GNP can also be believed to be boosted by the higher average oxidation state of Co ions as evidenced by XAS (Figure 4.10 (e)). The semi-crystalline nature of Co_3O_4/CeO_2/GNP is believed to boost charge transfer between the active crystalline counterpart Co_3O_4 and GNP, thereby strengthening metal-support interactions [47]. This, in turn, also enhances stability and durability as evidenced from CA and ADT tests. Another plausible reason behind generation of such a semi-crystalline nature could be from

the influence of the mild base urea added during synthesis. This predicament is based on the generation of highly crystalline similar CeO_2-based components [9,16,35] where the precipitating agent used was NaOH. Also, the crystallite sizes of those were also greatly larger than that reported in the present work. The synthesis route allows intricate alteration of electronic levels in the mixed Co_3O_4/CeO_2/GNP in a manner that boosts the electrocatalytic activity of Co_3O_4 in the mixed oxide without bringing any significant changes in the core crystal structures as evidenced by EXAFS. This aspect is presumed to play a role in preserving the inherent electrocatalytic nature of Co_3O_4 which is evidenced from the same $E_{onset,ORR}$ values (Table 4.6) for Co_3O_4/GNP and Co_3O_4/CeO_2/GNP.

4.2 Conclusions

CeO_2 paired with active Co_3O_4/GNP boosts generation of oxygen vacancy which in turn enhances ORR/OER performance. The facile Ce^{4+}/Ce^{3+} redox shuttle aids in faster shuttle between Co^{3+}/Co^{2+} which then consequently aids in faster and more efficient ORR and OER. Co_3O_4/CeO_2/GNP exhibits superior charge-transfer rates due to the presence of heterogeneous interfaces in comparison to the Co_3O_4/GNP, CeO_2/GNP and GNP as evidenced from the 'n' values. Its long-term durability can be validated from the minimal shift in $E_{1/2}$ in ADT even after 10,000 cycles endowing it as a robust electrocatalyst. This work paves the path for more exploration into CeO_2-based non-PGM electrocatalysts for potential replacement of precious metal catalysts in the near future.

References

[1] Muñoz, S. P. *Cobalt*. Retrieved on 20 Aug. 2024 from https://www.dailymetalprice.com/cobalt.html.

[2] Wang, S., Chen, S., Ma, L., and Zapien, J. A. Recent progress in cobalt-based carbon materials as oxygen electrocatalysts for zinc-air battery applications. *Materials Today Energy*, 20:1–31, 2021.

[3] Patowary, S., Chutia, B., Hazarika, K. K., and Bharali, P. Hybrid electrocatalysts with oxide/oxide and oxide/hydroxide interfaces for oxygen electrode reactions. In: Sudarsanam, P. , Yamauchi, Y. , and Bharali, P., editors, *Heterogeneous Nanocatalysis for Energy and Environmental Sustainability*. volume 1, Chap. XX, pages 111–132, ISBN: 9781394183517. John Wiley & Sons Ltd, 2022.

[4] Liu, Y., Ma, C., Zhang, Q., Wang, W., Pan, P., Gu, L., Xu, D., Bao, J., and Dai, Z. 2D Electron gas and oxygen vacancy induced high oxygen evolution performances for advanced Co_3O_4/CeO_2 nanohybrids. *Advanced Materials*, 31(21):1–9, 2019.

[5] Huang, J., Sheng, H., Ross, R. D., Han, J., Wang, X., Song, B., and Jin, S. Modifying redox properties and local bonding of Co_3O_4 by CeO_2 enhances oxygen evolution catalysis in acid. *Nature Communications*, 12(1):1–11, 2021.

[6] He, X., and Yi, X. Less active CeO_2 regulating bifunctional oxygen electrocatalytic activity of Co_3O_4@N-doped carbon for Zn–air batteries. *Journal of Material Chemistry A*, 7:6753–6765, 2019.

[7] Zhong, H., Alberto Estudillo-Wong, L., Gao, Y., Feng, Y., and Alonso-Vante, N. Oxygen vacancies engineering by coordinating oxygen-buffering CeO_2 with CoO_x nanorods as efficient bifunctional oxygen electrode electrocatalyst. *Journal of Energy Chemistry*, 59:615–625, 2021.

[8] Li, T., He, Z., Liu, X., Jiang, M., Liao, Q., Ding, R., and Liu, S. Interface interaction of Ag-CeO_2 -Co_3O_4 facilitate ORR/OER activity for Zn-air battery. *Surfaces and Interfaces*, 33:1–9, 2022.

[9] Liu, K., Huang, X., Wang, H., Li, F., Tang, Y., Li, J., and Shao, M. Co_3O_4-CeO_2/C as a highly active electrocatalyst for oxygen reduction reaction in Al-air batteries. *ACS Applied Materials & Interfaces*, 8(50):34422−34430, 2016.

[10] Guo, S., Wang, J., Sun, Y., Peng, L., and Li, C. Interface engineering of Co_3O_4/CeO_2 heterostructure in-situ embedded in Co/N-doped carbon nanofibers integrating oxygen vacancies as effective oxygen cathode catalyst for Li-O_2 battery. *Chemical Engineering Journal*, 452: 1–15, 2023.

[11] Morales, D. M., Kazakova, M. A., Dieckhöfer, S., Selyutin, A. G., Golubtsov, G. V., Schuhmann, W., and Masa, J. Trimetallic Mn-Fe-Ni Oxide nanoparticles supported on multi-walled carbon nanotubes as high-performance bifunctional ORR/OER electrocatalyst in alkaline media. *Advanced Functional Materials*, 30(6):1–12, 2020.

[12] Li, X., You, S., Du, J., Dai, Y., Chen, H., Cai, Z., Ren, N., and Zou, J. ZIF-67-derived Co_3O_4@carbon protected by oxygen-buffering CeO_2 as an efficient catalyst for boosting oxygen reduction/evolution reactions. *Journal of Materials Chemistry A*, 7(45):25853–25864, 2019.

[13] Han, X., He, G., He, Y., Zhang, J., Zheng, X., Li, L., Zhong, C., Hu, W., Deng, Y., and Ma, T. Y. Engineering catalytic active sites on cobalt oxide surface for enhanced oxygen electrocatalysis. *Advanced Energy Materials*, 8(10):1–13, 2018.

[14] Holder, C. F., and Schaak, R. E. Tutorial on powder x-ray diffraction for characterizing nanoscale materials. *ACS Nano*, 13(7):7359−7365, 2019.

[15] Goswami, C., Hazarika, K. K., Yamada, Y., and Bharali, P. Nonprecious hybrid metal oxide for bifunctional oxygen electrodes: endorsing the role of interfaces in electrocatalytic enhancement. *Energy & Fuels*, 35(16):13370–13381, 2021.

[16] Naebe, M., Wang, J., Amini, A., Khayyam, H., Hameed, N., Li, L. H., Chen, Y., and Fox, B. Mechanical property and structure of covalent functionalised graphene/epoxy nanocomposites. *Scientific Reports*, 4:1–7, 2014.

[17] Smyrnioti, M., and Ioannides, T. Synthesis of cobalt-based nanomaterials from organic precursors. In. Maaz, K., editor, *Cobalt*, pages 49–69, ISBN:978-953-51-3667-5. IntechOpen, Croatia, 2017.

[18] Zhang, F., Yuan, C., Lu, X., Zhang, L., Che, Q., and Zhang, X. Facile growth of mesoporous Co_3O_4 nanowire arrays on Ni foam for high performance electrochemical capacitors. *Journal of Power Sources*, 203:250–256, 2012.

[19] Nassar, M. Y., and Ahmed, I. S. Hydrothermal synthesis of cobalt carbonates using different counter ions: an efficient precursor to nano-sized cobalt oxide (Co_3O_4). *Polyhedron*, 30(15):2431–2437, 2011.

[20] Liu, F., Su, H., Jin, L., Zhang, H., Chu, X., and Yang, W. Facile synthesis of ultrafine cobalt oxide nanoparticles for high- performance supercapacitors. *Journal of Colloid and Interface Science*, 505:796–804, 2017.

[21] Patel, J., and Kiani, A. Comparative study of tribological behaviours of different base greases enhanced by graphene nano platelets. In: *Proceedings of the 3rd International Conference on Theoretical and Applied Nanoscience and Nanotechnology (TANN'19)*, pages 1–4, Ottawa, Canada, 2019.

[22] K. S. W. Sing. Reporting physisorption data for gas/solid systems with special reference to the determination of surface area and porosity (Recommendations 1984). *Pure and Applied Chemistry*, 57(4):603–619, 1985.

[23] Raja, P. M. V., and Barron, A. R. BET surface area analysis of nanoparticles. *Connexions project*, 1:1–6, 2011.

[24] Dwivedi, A., Sharma, B. K., Rajagopalan, N., and Sinha, S. Hydrothermal decomposition of cobalt hydroxide in saturated water vapor. *Industrial & Engineering Chemistry Research*, 59: 491-496, 2020.

[25] Zhang, S., and Wang, C. Precise analysis of nanoparticle size distribution in TEM Image. *Methods and protocols*, 6(4):1-6, 2023.

[26] Kim, K. H., and Choi, Y. H. Surface oxidation of cobalt carbonate and oxide nanowires by electrocatalytic oxygen evolution reaction in alkaline solution. *Materials Research Express*, 9(3):34001, 2022.

[27] Duan, Q., and Chen, H. Synthesis and electrochemical properties of Co_3O_4 nanoparticles by hydrothermal method at different temperatures. *IOP Conference Series: Materials Science and Engineering*, 207:1–8, 2017.

[28] Ma, R., Jahurul Islam, M., Amaranatha Reddy, D., and Kim, T. K. Transformation of CeO_2 into a mixed phase CeO_2/Ce_2O_3 nanohybrid by liquid phase pulsed laser ablation for enhanced photocatalytic activity through Z-scheme pattern. *Ceramics International*, 42(16):18495–18502, 2016.

[29] Vazirov, R. A., Sokovnin, S. Y., Ilves, V. G., Bazhukova, I. N., and Kuznetsov, N. P. M. V. Physicochemical characterization and antioxidant properties of cerium oxide nanoparticles. *Journal of Physics*: *Conference Series*, 1115(3):1–6, 2018.

[30] Ravel, B., and Newville, M. ATHENA and ARTEMIS: Interactive graphical data analysis using IFEFFIT. *Physica Scripta*, 2005(T115):1007–1010, 2005.

[31] Ravel, B., and Newville, M. ATHENA and ARTEMIS. In: Chantler, C. T., Boscherini, F., Bunker, B., editors, *X-Ray Absorption Spectroscopy and Related Techniques*. volume 1 of *International Union of Crystallography*, pages 1–5, ISBN: 978-1-119-43394-1. John Wiley & Sons, England, 2020.

[32] Yildirim, B., and Riesen, H. Coordination and oxidation state analysis of cobalt in nanocrystalline $LiGa_5O_8$ by X-ray absorption spectroscopy. *Journal of Physics: Conference Series*, 430(1):1–4, 2012.

[33] Chou, S. C., Tso, K. C., Hsieh, Y. C., Sun, B. Y., Lee, J. F., and Wu, P. W. Facile synthesis of Co_3O_4@CoO@Co gradient core@shell nanoparticles and their applications for oxygen evolution and reduction in alkaline electrolytes. *Materials*, 13(12):1–14, 2020.

[34] Lv, L., Zha, D., Ruan, Y., Li, Z., Ao, X., Zheng, J., Jiang, J., Chen, H. M., Chiang, W. H., Chen, J., and Wang, C. A Universal method to engineer metal oxide-metal-carbon interface for highly efficient oxygen reduction. *ACS Nano*, 12(3):3042−3051, 2018.

[35] Hazarika, K. K., Yamada, Y., Matus, E. V., Kerzhentsev, M., and Bharali, P. Enhancing the electrocatalytic activity via hybridization of Cu(I/II) oxides with Co_3O_4 towards oxygen electrode reactions. *Journal of Power Sources*, 490:229511, 2021.

[36] Liu, R., Xian, Z., Zhang, S., Chen, C., Yang, Z., Li, H., Zheng, W., Zhang, G., and Cao, H. Electrochemical-reduction-assisted assembly of ternary Ag nanoparticles/ polyoxometalate/graphene nanohybrids and their activity in the electrocatalysis of oxygen reduction. *RSC Advances*, 5(91):74447−74456, 2015.

[37] Chutia, B., Patowary, S., Misra, A., Rao, K. N., and Bharali, P. Morphology effect of Co_3O_4 nanooctahedron in boosting oxygen reduction and oxygen evolution reactions. *Energy & Fuels*, 36:13863−13872, 2022.

[38] Goswami, C., Yamada, Y., Matus, E. V., Ismagilov, I. Z., Kerzhentsev, M., and Bharali, P. Elucidating the role of oxide-oxide/carbon interfaces of CuO_x-CeO_2/C in boosting electrocatalytic performance. *Langmuir*, 36(49):15141−15152, 2020.

[39] Chutia, B., Hussain, N., Puzari,P., Jampaiah, D., Bhargava, S. K., Matus, E. V., Ismagilov, I. Z., Kerzhentsev, M., and P. Bharali. Unraveling the role of CeO_2 in stabilization of multivalent Mn Species on α-MnO_2/Mn_3O_4/CeO_2/C surface for enhanced electrocatalysis. *Energy & Fuels*, 35(13):10756−10769, 2021.

[40] Chutia, B., and Bharali, P. Oxygen deficient interfacial effect in CeO_2-modified Fe_2O_3/C for oxygen reduction reaction in alkaline electrolyte. *Catalysis Communications*, 164:1−5, 2022.

[41] Xie, J., Zhao, Z., Coker, V. S., O'Driscoll, B., Cai, R., Haigh, S. J., Holmes, S. M., and Lloyd, J. R. Bioproduction of cerium-bearing magnetite and application to improve carbon-black supported platinum catalysts. *Journal of Nanobiotechnology*, 22(1):1−14, 2024.

[42] Dupont, M., Hollenkamp, A. F., and Donne, S. W. Electrochemically active surface area effects on the performance of manganese dioxide for electrochemical capacitor applications. *Electrochimica Acta*, 104:140−147, 2013.

[43] Zhong, H., Estudillo-wong, L. A., Gao, Y., Feng, Y., and Alonso-vante, N. Oxygen vacancies engineering by coordinating oxygen-buffering CeO_2 with CoO_x nanorods as

efficient bifunctional oxygen electrode electrocatalyst. *Journal of Energy Chemistry*, 59:615–625, 2021.

[44] Co_3O_4−CeO_2/C as a highly active electrocatalyst for oxygen reduction reaction in Al−air batteries. *ACS Applied Materials & Interfaces*, 8:34422−34430, 2016.

[45] Yang, W. Co_3O_4 nanofibers compounded with Pt/C as efficient bifunctional electrocatalysts for rechargeable Zn-air battery. *Journal of Materials Science*: *Materials in Electronics*, 34(10):1–11, 2023.

[46] Tao, Z., Zhao, H., Lv, N., Luo, X., Yu, J., Tan, X., and Mu, S. Crystalline/amorphous-Ru/VO_x phase engineering expedites the alkaline hydrogen evolution kinetics. *Advanced Functional Materials*, 34(19):1–8, 2024.